Published in final edited form as:
J Aerosol Sci. 2012 April ; 46: 7–19. doi:10.1016/j.jaerosci.2011.11.005.

Aggregate Morphology Evolution by Sintering: Number & Diameter of Primary Particles

Max L. Eggersdorfer[1], **Dirk Kadau**[2], **Hans J. Herrmann**[2], and **Sotiris E. Pratsinis**[1,*]

[1]Particle Technology Laboratory, Institute of Process Engineering, Department of Mechanical and Process Engineering, ETH Zurich, Sonneggstrasse 3, CH-8092 Zürich, Switzerland.

[2]Computational Physics of Engineering Materials, Institute of Building Materials, Department of Civil, Environmental and Geomatic Engineering, ETH Zurich, Schafmattstrasse 6, CH-8093 Zürich, Switzerland. Ph. +41 (0) 44 633 27 01; Fax. +41 (0) 44 633 11 47 dkadau@ethz.ch, hans@ifb.baug.ethz.ch

Abstract

The structure of fractal-like agglomerates (physically-bonded) and aggregates (chemically- or sinter-bonded) is important in aerosol synthesis of nanoparticles, and in monitoring combustion emissions and atmospheric particles. It influences also particle mobility, scattering, and eventually performance of nanocomposites, suspensions and devices made with such particles. Here, aggregate sintering by viscous flow of amorphous materials (silica, polymers) and grain boundary diffusion of crystalline ceramics (titania, alumina) or metals (Ni, Fe, Ag etc.) is investigated. A scaling law is found between average aggregate projected area and equivalent number of constituent primary particles during sintering: from fractal-like agglomerates to aggregates and eventually compact particles (e.g. spheres). This is essentially a relation independent of time, material properties and sintering mechanisms. It is used to estimate the equivalent primary particle diameter and number in aggregates. The evolution of aggregate morphology or structure is quantified by the effective fractal dimension (D_f) and mass-mobility exponent (D_{fm}) and the corresponding prefactors. The D_{fm} increases monotonically during sintering converging to 3 for a compact particle. Therefore D_{fm} and its prefactor could be used to gauge the degree or extent of sintering of agglomerates made by a known collision mechanism. This analysis is exemplified by comparison to experiments of silver nanoparticle aggregates sintered at different temperatures in an electric tube furnace.

Keywords

Aggregate; grain boundary diffusion; fractal dimension; mass-mobility exponent; primary particle size

1 Introduction

Nanoparticle production in the gas phase is a well-established route for carbon black, pigmentary titania and fumed silica (Ulrich, 1984) and a promising method for many new, sophisticated materials like catalysts, sensors, phosphors, biomaterials and even nutritional products (Strobel & Pratsinis, 2007). Such particles grow by gas and surface reaction, coagulation and sintering and tend to form fractal-like aggregates and agglomerates.

[*]Corresponding author Ph. +41 (0) 44 632 31 80; Fax. +41 (0) 44 632 15 95 pratsinis@ptl.mavt.ethz.ch. meggers@ptl.mavt.ethz.ch

Europe PMC Funders Author Manuscripts

Although models exist to characterize agglomerates of spherical particles (Lall & Friedlander, 2006), in practice, particles often partially coalesce upon collision forming aggregates with sinter necks (Koch & Friedlander, 1990). The resulting structures are more compact (Akhtar et al., 1994) than those predicted by particle collision alone (Schaefer & Hurd, 1990). Aerosol-generated fractal-like particles have typically an effective fractal dimension (Schaefer & Hurd, 1990; Hyeon-Lee et al., 1998) D_f = 1.6 to 2.5 or mass-mobility exponent (Kim et al., 2009; Scheckman et al., 2009) D_{fm} = 1.8 to 2.9. A D_f of around 1.8 or 1.9 corresponds to open structured agglomerates generated by diffusion-limited (DLCA, Kolb & Herrmann, 1987) or ballistic cluster-cluster agglomeration (BCCA, Tence et al., 1986). A D_f larger than 1.8 for particles made by DLCA can be attributed to aggregate sintering (Akhtar et al., 1994) that may lead to fully compact (D_f = 3) particles as has been measured by *in-situ* small angle X-ray scattering in laminar diffusion flames (Camenzind et al., 2008). A D_f lower than 1.8 can be attributed to primary particle polydispersity which monotonically decreases D_f (Eggersdorfer & Pratsinis, 2012).

Agglomerate and aggregate morphology and primary particle size strongly affect aerosol behavior and properties. The aerosol mobility in the free molecular (Meakin, 1988) and transition (Rogak et al., 1993) regime depends on structure, number and diameter of constituent primary particles (Sorensen, 2011). Besides particle transport, also energy (heat) transfer is determined by primary particle size and agglomerate/aggregate morphology (Filippov et al., 2000). The light scattering and absorption of open-structured aerosol agglomerates (D_f < 2) is a function of structure and primary particle size (Sorensen, 2001). Some of the chemically most active sites are thought to be at particle necks, the so-called 3-phase boundaries. Furthermore the mechanical stability of nanoparticle layers (Tricoli et al., 2008a), electron transport and sensitivity of gas sensors (Tricoli et al., 2008b) and electrical conductivity (Riefler & Madler, 2010) are significantly influenced by constituent primary particle and aggregate size (Keskinen et al., 2009) and degree of sintering.

Here the evolution of particle coalescence by viscous flow sintering (e.g. SiO_2, polymers) and grain boundary diffusion (e.g. TiO_2, metals) of agglomerates consisting of 16 – 512 primary particles is monitored in detail: from fractal-like agglomerates to aggregates to eventually compact spheres (Eggersdorfer et al., 2011). The focus is on projected aggregate surface area (a_a), mobility diameter (d_m), radius of gyration (r_g) and aggregate morphology (D_f, D_{fm}) in the free molecular and transition regime where nanoparticle sintering typically takes place at high process temperatures (Tsantilis & Pratsinis, 2004; Heine & Pratsinis, 2007). A scaling between number of primary particles, n_p, and a_a (Medalia, 1967) is combined with the relation between a_a and d_m (Meakin, 1988) to calculate the average number and diameter of primary particles in aggregates. That way the evolution of D_f (r_g-based) and D_{fm} (d_m-based) and prefactors are investigated during sintering as they are used to characterize fractal-like particles by light scattering (Schaefer & Hurd, 1990; Hyeon-Lee et al., 1998; Sorensen, 2001) and mass-mobility (Park et al., 2003) measurements. This method is applied to sintering of silver aggregates (Kim et al., 2009) to estimate their degree of sintering as they have been characterized by mass-mobility measurements.

2 Theory

Fractal-like agglomerates and aggregates are typically characterized by their average primary particle and mobility-equivalent diameters. The mobility-equivalent agglomerate diameter in the free molecular (Meakin, 1988) and transition regimes (Rogak et al., 1993) is the diameter of a sphere having the equivalent projected area as the agglomerate. Additionally agglomerate structure is described by power laws between its characteristic size and mass or number of its primary particles. Since aerosol agglomerates contain commonly up to a few thousand primary particles, such agglomerates might be too small for

a formal asymptotic scaling over several orders of magnitude. Therefore these power law exponents and prefactors have to be considered as effective and agglomerates just fractal-like. A summary of such scaling laws for agglomerates and aggregates is given here.

2.1 Projected Area-based Scaling

The volume - surface equivalent primary particle diameter d_{va} (surface area mean diameter) and number n_{va} in agglomerates or aggregates of volume v and surface area a are (Kruis et al., 1993):

$$d_{va}=\frac{6v}{a}, \quad (1)$$

$$n_{va}=\frac{v}{\pi d_{va}^3/6}. \quad (2)$$

For agglomerates with monodisperse, spherical primary particles in point contact, eqs. 1 and 2 give the real primary particle diameter d_p and number n_p. For practical systems, d_{va} is the equivalent primary particle diameter determined by gas (e.g. nitrogen) adsorption, d_{BET}, or by small angle X-ray scattering (Hyeon-Lee et al., 1998), $d_{V/S}$. The average projected area a_a of fractal-like agglomerates of monodisperse primary particles can be related to n_p by a power law (Medalia, 1967):

$$n_p=k_a\left(\frac{a_a}{a_p}\right)^{D_a}, \quad (3)$$

where $a_p=\pi d_p^2/4$ is the projected area of a primary particle and k_a and D_a are parameters describing agglomerate structure that are extracted from experimental (Megaridis & Dobbins, 1990; Koylu & Faeth, 1992) or numerical (Medalia, 1967; Al Zaitone et al., 2009) studies.

2.2 Radius of Gyration Scaling

The agglomerate mass m is related to the ratio of radius of gyration, r_g, over the primary particle radius, r_p (= d_p/2) by (Sutherland & Goodarz-Nia, 1971):

$$m=k_f\left(\frac{r_g}{r_p}\right)^{D_f}, \quad (4)$$

where k_f is a prefactor and the exponent D_f is the mass fractal dimension. The r_g of a fractal-like particle is its root mean-square radius (Jullien & Botet, 1987):

$$r_g^2=\frac{\int\rho(r)\,r^2dr}{\int\rho(r)\,dr}, \quad (5)$$

where $\rho(r)$ is the radial density distribution. The mass of agglomerates of monodisperse, spherical primary particles is: $m=n_p\cdot(4/3)\,\pi r_p^3\rho$ and eq. 4 is equivalent to the number-size relation (Mandelbrot, 1982):

$$n_p=k_n\left(\frac{r_g}{r_p}\right)^{D_f}, \quad (6)$$

where $k_n = k_f / \left(\rho \pi d_p^3/6\right)$.

2.3 Mobility Diameter Scaling

The mobility-equivalent diameter d_m of an agglomerate in the free molecular (Meakin, 1988) and transition regime (Rogak et al., 1993) is:

$$d_m = \sqrt{\frac{4a_a}{\pi}}. \quad (7)$$

This can be measured by a differential mobility analyzer (DMA, Knutson & Whitby, 1975) and the agglomerate mass m can be obtained with an aerosol particle mass (APM) analyzer (Ehara et al., 1996). The agglomerate volume is calculated with the known material density: $v = m/\rho$. Hence the equivalent primary particle diameter can be estimated by combining eqs. 1 – 3, 7 as a function of measured d_m and v:

$$d_{va} = \frac{6v}{a} = \left(\frac{\pi k_a}{6v}(d_m)^{2D_\alpha}\right)^{1/(2D_\alpha - 3)}. \quad (8)$$

The d_{va} corresponds to the average primary particle size (eq. 1) for “ideal” agglomerates of polydisperse spherical primary particles (no sinter necks) and to the volume to surface area ratio for aggregates.

The agglomerate mobility diameter d_m can be related to its mass by (Park et al., 2004):

$$m = k_{fm}\left(\frac{d_m}{d_p}\right)^{D_{fm}}. \quad (9)$$

The exponent D_{fm} might be simplistically identified with D_f (Scheckman et al., 2009) but the two are not exchangeable since $d_m \neq 2r_g$ as shown below. Here, the D_{fm} is referred to as mass-mobility exponent. The mass in eq. 9 can be substituted as well by n_p for agglomerates of monodisperse, spherical primary particles like in eq. 6:

$$n_p = k_m\left(\frac{d_m}{d_p}\right)^{D_{fm}}, \quad (10)$$

where $k_m = k_{fm} / \left(\rho \pi d_p^3/6\right)$. For example, agglomerates of monodisperse primary particles made by DLCA have a $D_f = 1.79 \pm 0.03$ and $k_n = 1.39 \pm 0.06$ (Eggersdorfer et al., 2011) consistent with Meakin (1988). The same agglomerates have $D_{fm} = 2.15 \pm 0.003$ and $k_m = 1.11 \pm 0.01$ and $D_\alpha = D_{fm}/2 = 1.075 \pm 0.0021$ and $k_a = k_m$ in agreement with Sorensen (2011). Clearly the difference between D_f and D_{fm} depends on the relation between r_g and d_m as it will be elucidated here.

2.4 Aggregate Multiparticle Sintering Model

Agglomerates containing initially $n_{p,0} = 16$-512 particles are generated by a hierarchical cluster-cluster agglomeration mechanism (Botet et al., 1984). These agglomerates are sintered to aggregates by viscous flow (Eggersdorfer et al., 2011) and grain boundary diffusion (Appendix). Different sintering mechanisms are studied to investigate their effect on aggregate properties. The driving force for sintering is the minimization of free energy. For amorphous materials (e.g. silica, polymers), this minimization results in a viscous flow and reduction of surface area. In crystalline materials (e.g. titania, alumina, Ag, Ni) a grain boundary forms between misaligned crystals. The stress gradient between neck center and

surface causes a flux of atoms into the neck (Coble, 1958; Rahaman, 2008) resulting in a reduction of aggregate surface area. The primary particle centers approach each other and both mechanisms end in full coalescence.

The change in particle distance dx/dt and particle growth rate dr_p/dt are calculated by energy and mass balances (Eggersdorfer et al., 2011). The evolution of the resulting average projected aggregate area a_a, D_f, D_{fm}, k_n, k_m, d_m, r_g as well as average primary particle d_{va} and n_{va} are monitored. The a_a is calculated with Monte-Carlo integration (Meakin, 1988) and averaged over 50 agglomerates or aggregates of each $n_{p,0}$ taken at 50 homogeneously distributed random angles for each agglomerate/aggregate.

3 Results and Discussion

3.1 Validation of Aggregate Sintering Dynamics

The present multiparticle aggregate surface area evolution by viscous flow sintering is consistent with literature for two equal and unequal particles as well as for chain and irregular aggregates (Eggersdorfer et al., 2011). Initial neck growth and shrinkage rate of two spherical particles of initial radius $r_{p,0}$ during sintering scales as (Rahaman, 2008):

$$\left(\frac{R}{r_{p,0}}\right)^y = \frac{B}{\left(r_{p,0}\right)^w} t, \quad (11a)$$

$$\left(\frac{\Delta x}{x_0}\right)^{y/2} = -\frac{B}{2^y \left(r_{p,0}\right)^w} t \quad (11b)$$

where R is the neck radius, y and w are exponents depending on sintering mechanism, B is a constant depending on material and geometrical parameters and x is the particle center to neck distance (Fig. 1). The present algorithm was validated by comparing the evolution of R to eq. 11a,b with $B = 3\gamma/2\eta$ and $B = 96 D_v \delta_{gb} \gamma \Omega / k_B T$ for viscous flow and grain boundary diffusion, respectively (Rahaman, 2008), where γ is the surface energy, η the viscosity, D_v the vacancy diffusion coefficient, δ_{gb} the grain boundary thickness, Ω the volume of an atom or vacancy, k_B the Boltzmann constant and T the temperature. For grain boundary diffusion, the exponents were calculated to be $y = 6$ and $w = 4$ consistent with Coble (1958), while for viscous flow sintering, $y = 2$ and $w = 1$ consistent with Frenkel (1945) and Wolf et al. (2012).

3.2 Aggregate Projected Area, a_a

Figure 2 shows the evolution of particle morphology during sintering by grain boundary diffusion with normalized time $t/\tau_{0,gb}$ ($\tau_{0,gb}$ is the characteristic time for sintering by grain boundary diffusion, Appendix A.2) for a representative agglomerate of 512 primary particles, initially. Upon the onset of sintering, necks are developed between primary particles so the agglomerates become aggregates and their constitutive primary particle diameters increase similar to sintering by viscous flow (Fig. 5 in Eggersdorfer et al., 2011). Initially, the driving force for sintering is largest with the steepest curvature at particle necks. Later on, the aggregate shrinks ($t/\tau_{0,gb} > 8.2$) and finally evolves to a spherical particle (here at $t/\tau_{0,gb} = 1.3 \cdot 10^5$).

The effect of sintering mechanism on aggregate geometry during sintering is investigated. Figure 3 shows the relation (eq. 3) between normalized projected aggregate area, a_a/a_p, and average number of primary particles, n_{va}, during aggregate coalescence or sintering by a)

Europe PMC Funders Author Manuscripts

grain boundary diffusion (Fig. 2) and b) viscous flow (Fig. 5 in Eggersdorfer et al., 2011). For a given starting agglomerate or aggregate, a_a, a_p and n_{va} are determined by the corresponding sintering model at any time t resulting in a point in Fig. 3a or 3b. Only for the initial agglomerates $n_{va} = n_p$ as the primary particles are monodisperse and in point contact. As expected for both sintering mechanisms, n_{va} decreases and d_{va} increases during sintering. At the end of sintering or coalescence $n_{va} = a_a/a_p = 1$. Equation 3 fits remarkably well ($R^2 = 0.998$) these data resulting in the corresponding D_α and k_a for each sintering mechanism.

Although eq. 3 was proposed originally for agglomerates of non-coalescing monodisperse primary particles with $n_p = n_{va}$ (Medalia, 1967), Figure 3 shows that it holds well also for aggregates undergoing sintering that result in polydisperse primary particles and an evolving structure (D_f, D_{fm}) consistent with Al Zaitone et al. (2009). The parameters of eq. 3 are $k_a = 0.990 \pm 0.004$ and $D_\alpha = 1.070 \pm 0.003$ for grain boundary diffusion sintering (Fig. 3a) and $k_a = 1.0065 \pm 0.0024$ and $D_\alpha = 1.068 \pm 0.0014$ for viscous flow sintering (Fig. 3b). The difference in k_a and D_a between viscous flow and grain boundary diffusion is rather minor and quite close to the error of their regressions as shown in Figure 3. Although the neck growth rate (or approach of particle centers) depends linearly on the primary particle size for viscous flow (eq. 11: $w = 1$) and to the fourth power for grain boundary diffusion sintering (eq. 11: w = 4, Wolf et al., 2012), the k_a and D_a are basically the same. So average values ($k_a = 0.998$ and $D_\alpha = 1.069$) can be used to estimate the a, d_{va} and n_{va} in aggregates from eq. 8 that are used in mass-mobility measurements. So only the temporal evolution of n_{va} and d_{va} depends on sintering mechanism while the geometric relations during sintering are independent of that mechanism as long as the material is isotropic or averaged over several crystal orientations (Buesser et al., 2011). Often, nanoparticles consist of more than 512 primary particles and one can extrapolate to larger aggregates because fractality is strictly defined only in the limit of infinitely large sizes.

3.3 Evolution of Mobility, d_m, and Average Primary Particle Diameter, d_{va}, during Sintering

Figure 4 shows the evolution of d_{va} (eq. 8) and d_m of agglomerates undergoing viscous flow sintering and having initial $D_f = 1.79$, $d_{p,0} = 20$ nm and $n_{p,0} = 16$ (broken line), 64 (dot-broken line), 256 (double-dot broken line) and 512 (dotted line). Most importantly, the direct relation between d_m and d_{va} during sintering is shown and compared to experiments in section 3.6. Initially the d_{va} is set to $d_{p,0} = 20$ nm for all agglomerates depicted by the agglomerate or collision (horizontal thin solid) line (Fig. 2 in Xiong & Pratsinis, 1993). During sintering, every d_m decreases as necks form and primary particles grow (Fig. 2) while their total surface area decreases. For example, the d_m of agglomerates containing 64 primary particles (dot-broken line) decreases from 150 nm to $d_m = d_{va} = d_p = 80$ nm, the size of the fully coalesced sphere upon completion of sintering or coalescence. So the aggregate progressively densifies, until completely compact ($d_m = d_p$) structures are formed as observed experimentally for nanoparticle sintering (Tsyganov et al., 2007) and the limit of $n_{va} = n_p = 1$ is reached for fully coalesced particles, given by the diagonal (solid bold) coalescence line (Fig. 2 in Xiong & Pratsinis, 1993).

Similar results are obtained for sintering by grain boundary diffusion. Figure 4 reveals that the relationship between d_{va} and d_m hardly depends on sintering mechanism (similar k_a and D_α). At a given d_m, aggregates that sinter by viscous flow or grain boundary diffusion have the same volume to surface ratio and thus the same average primary particle size, d_{va} (eq. 1). The actual time, however, to reach this d_m or d_{va} depends on sintering mechanism, material properties and temperature. For example, titania will reach a much larger size than silica undergoing sintering at the same initial and process conditions (high temperature residence time) as has been shown experimentally and theoretically (Xiong et al., 1993).

The driving force for sintering (particle curvature and excess surface area) decreases exponentially as aggregates coalesce to more compact structures (e.g. sphere, Fig. 6 in Eggersdorfer et al., 2011). So d_{va} increases rapidly at the start of sintering. During the final stage, an oval aggregate transforms into a sphere very slowly ($t/\tau_{0,gb}$ = 6272 - $1.3{\cdot}10^5$, Fig. 2). This stage takes much, much longer than the initial neck growth stage ($t/\tau_{0,gb}$ = 0 - 0.7, Fig. 2) consistent with molecular dynamics of the full coalescence or sintering of TiO_2 nanoparticles of 2 - 5 nm in initial diameter (Buesser et al., 2011).

Figure 4 shows also three snapshots of the progress of viscous flow sintering at $t/\tau_{0,vis}$ = 0, 1 (squares) and 6 (circles) for the agglomerate of $n_{p,0}$ = 256 (Eggersdorfer et al., 2011). This progress is similar for the other $n_{p,0}$ as well as for sintering by grain boundary diffusion (Fig. 2). At $t/\tau_{0,vis}$ = 1 (squares), the average primary particle diameter is nearly independent of initial agglomerate size as all symbols are almost on the same horizontal line. At this $t/\tau_{0,vis}$, only the d_{va} of aggregates with $n_{p,0}$ = 16 is slightly smaller since they have approached their diameter at full coalescence ($d_m = d_{va}$) at $t/\tau_{0,vis}$ = 6 (circles). Larger aggregates ($n_{p,0}$ > 16) lag behind in structure evolution even though they have reached larger equivalent primary particle diameters, d_{va}. For these aggregates ($n_{p,0}$ > 16), the d_{va} is still almost independent of initial agglomerate size at $t/\tau_{0,vis}$ = 6. This indicates that two-particle interactions dominate the evolution of d_{va} almost up to full coalescence as fractal-like clusters made by cluster-cluster agglomeration have predominantly a coordination number $z \approx 2$ independent of $n_{p,0}$ (here: z = 1.89 for $n_{p,0}$ = 16, z = 1.98 for $n_{p,0}$ =64 and z = 2.01 for both $n_{p,0}$ = 256 and 512), consistent with Hasmy et al. (1993). Since d_{va} is almost independent of d_m even for highly sintered aggregates for sufficiently large aggregates, measuring only a few data points (d_m, m) suffice to estimate d_{va} and the specific surface area (a/m) by eq. 8 replacing m by v using the particle density.

3.4 Mobility Radius and Radius of Gyration

The mobility radius $r_m = d_m/2$ can be accurately obtained by DMA measurements but depends on aggregate orientation in the flow field, the size regime, etc. and hence is an extrinsic property of the aggregate. In contrast, r_g describes the arrangement of mass within the aggregate and is an intrinsic property (Sorensen, 2011) which can be measured by microscopy or static light scattering. Obtaining r_g is important also for determining the correct collision frequency of fractal-like particles that is needed in design of aerosol processes for synthesis, conditioning and collection of these particles.

Figure 5a shows the evolution of the ratio r_m/r_g during viscous sintering of agglomerates consisting of 16-512 primary particles by multiparticle sintering simulations. For large aggregates ($n_{p,0}$ > 16), the r_m/r_g decreases as particle centers come closer during initial neck formation. The primary particle radii are increased resulting in a slight change of r_g. The projected area, however, decreases by neck formation, so r_m decreases continuously (eq. 7). These effects lead initially to a faster reduction of r_m than r_g resulting in a minimum in r_m/r_g which later on increases and finally converges nicely to the asymptotic limit (Hiemenz, 1986) of a fully coalesced sphere of $\sqrt{5/3}$. The minimum in r_m/r_g is more pronounced for larger aggregates and not existent for $n_{p,0}$ = 16. The r_g of the aggregates with $n_{p,0}$ > 16 is rather constant during initial neck formation (Fig. 6c in Eggersdorfer et al., 2011) while it instantly decreases for $n_{p,0}$ = 16 and thus has no minimum. Clearly, r_m/r_g depends on aggregate size and degree of sintering as indicated above.

Figure 5b shows the evolution of the ratio r_m/r_g with n_{va} during sintering. The n_{va} decreases continuously as primary particles grow until full coalescence is reached (n_{va} = 1). For one particle (diamond) and two particles with point contact (circle), exact results are known (Sorensen, 2011). The correct n_{va} = 1 limit is obtained for all fully coalesced spheres. The

$n_{va} = 2$ limit, however, is not reached as particles undergoing sintering reach an oval shape, $t/\tau_{0,gb} = 6272$ (Fig. 2) rather than that of two spherical particles with a point contact.

3.5 Evolution of Fractal Dimension, Mass-Mobility Exponent and their Prefactors

The morphology of fractal-like agglomerates formed by collisions of spherical primary particles can be characterized by power laws between a characteristic size and mass or number of primary particles (eq. 4, 6, 9, 10). These power laws are applied to aggregates during sintering to describe their change in morphology. Figure 6 shows the evolution of a) average mass-mobility exponent (D_{fm}, circles) and effective fractal dimension (D_f, triangles) and b) their prefactors during viscous flow sintering of initially 16-512 primary particles averaged over 50 aggregates each. This is done similarly to experimental characterization of agglomerates by light scattering (Sorensen et al., 1992) and DMA-APM (Scheckman et al., 2009). The r_m or r_g of differently sized aggregates is log-log plotted against their mass and the slope of the line corresponds to D_{fm} or D_f, respectively, while the intersection with the y-axis is the logarithm of the prefactor k_m or k_n (eq. 10 and 6), respectively (Eggersdorfer et al., 2010). The r_g and r_m are normalized by the initial r_p and the mass is normalized by the initial m_p at $t = 0$. Similar results are obtained for sintering by grain boundary diffusion (Fig. 3b).

The D_f (Fig. 6a, triangles) decreases as small aggregates sinter faster having a faster reduction of r_g (Fig. 6c in Eggersdorfer et al., 2011). This results in a minimum of D_f (eq. 6), consistent with small-angle X-ray scattering (SAXS) monitoring of silica nanoparticle aggregate sintering (Camenzind et al., 2008), before reaching $D_f = 3$ at full coalescence. The reduction in D_f means a smaller mass-r_g slope that leads to a larger k_n (Fig. 6b, triangles) which peaks at $t/\tau_0 = 7$ where D_f reaches its minimum. An increase in k_n corresponds to a reduced anisotropy for ideal agglomerates without sinter necks (Heinson et al., 2010). The r_g of a compact sphere is $\sqrt{3/5}r_p$ asymptotically resulting in $k_n = (5/3)^{3/2}$ for $n_{va} = 1$. So the k_n of the perfectly symmetric compact sphere at the end of sintering is higher ($k_n = 2.2$ at $t/\tau_0 = 80$ in Fig. 6b) than that of the initial agglomerate ($k_n = 1.39$) consistent with Heinson et al. (2010). The observed maximum in k_n and minimum in D_f correspond to the formation of elongated aggregates during the early stages of sintering ($t/\tau_{0,gb} = 0.7 – 18$ by grain boundary diffusion, Fig. 2) as has been shown also for viscous flow sintering (Fig. 8 in Eggersdorfer et al., 2011).

In contrast to D_f, the mobility-based D_{fm} (Fig. 6a, circles) continuously increases until it reaches also the asymptotic value of 3 for compact particles (e.g. spheres). The difference between D_{fm} and D_f depends on the relation between r_m and r_g (Fig. 5). The r_g hardly changes during initial neck formation and restructuring while the projected area and thus r_m are immediately affected for all aggregate sizes as discussed with Fig. 5. So the D_{fm} does not reach a minimum but increases monotonically while the decreasing r_m results also in an increase in the prefactor k_m (Fig. 6b, circles). The k_m is more sensitive to neck formation at the beginning of sintering and increases while D_{fm} is still almost constant for $t/\tau_0 < 1$. The k_m converges to 1, since the radius of the fully sintered sphere is $N^{1/3}r_0$ at $D_{fm} = 3$ and the normalized mass is $m/m_p = N$. The mobility-based D_{fm} is the only characteristic of aggregate structure discussed here which has a monotonic behavior and could be used to quantify the degree or extent of sintering for aggregates made by a known mechanism to choose the correct D_a and k_a (e.g. cluster-cluster collisions as in coagulation).

3.6 Application to Experimental Data

3.6.1 Average Primary Particle Diameter d_{va} and Number n_{va} from Mass-Mobility Measurements—The present geometric relations of aggregates (eq. 3 & 8) are

used to analyze experimental data to gain insight of aggregate morphology and quantitative understanding of the degree or extent of sintering by *in-situ* measurements. This is feasible since k_a and D_a are constant during sintering and practically independent of sintering mechanism (Fig. 3). Kim et al. (2009) generated silver nanoparticle agglomerates by evaporation/condensation within an electric tube furnace and sintered them “in flight” through a second furnace at 20 – 600 °C. The agglomerates were mobility-size segregated by DMA before the average mass m of a size-selected d_m was measured with an APM. The measured d_m and m by Kim et al. (2009) are employed in eq. 8 to calculate d_{va}.

Figure 7 shows the average primary particle a) diameter, d_{va}, and b) number, n_{va}, of eq. 2 & 8 (symbols) as a function of d_m from Table 1 of Kim et al. (2009). The volume v for eq. 8 is calculated with the measured aggregate mass m and density of silver ($\rho = 10.5 \cdot 10^3$ kg/m^3) while the average k_a and D_a from Fig. 3 are used to calculate d_{va}. Figure 7a compares these d_{va} to the primary particle diameter, d_{TEM}, from counting TEM images (Fig. 8 in Kim et al., 2009) after converting it from number- to surface-average mean diameter (broken line). The grey area corresponds to the measured standard deviation ($\sigma = 3.1$ nm) of d_{TEM} at $T = 20$ °C. The d_{va} of the present work at 20 °C (triangles, eq. 8) are in reasonable agreement with d_{TEM}.

Figure 7b shows that the aggregates at 20 °C with $d_m = 100$ nm consist, on average, of 60 primary particles and aggregates with $d_m = 300$ nm of 730 particles (triangles, Fig. 7b). The primary particles (volume to surface area ratio) grew larger for higher sintering temperatures within the same residence time in the furnace. The characteristic sintering time τ_0 decreases with increasing temperature, so t/τ_0 increases and the sintering evolves further. Note that the measurements were taken at fixed mobility diameters between 50 - 300 nm (Table 1 in Kim et al., 2009) and do not represent the sintering evolution of d_m for a single aggregate of a given initial size as shown in Fig. 4. At 100 °C (circles), the increase in d_{va} (Fig. 7a) and reduction in n_{va} (Fig. 7b) is small, similar to that of 20 °C consistent with Kim et al. (2009: Table 1).

At 200 °C (squares) substantial sintering and primary particle growth took place in qualitative agreement with particle images (Fig. 7c,d in Kim et al., 2009) which show strongly sintered aggregates. Nonetheless d_{va} is nearly independent of aggregate mobility diameter (Fig. 7a). The smallest Ag aggregates at $d_m = 50$ nm have 5 – 7 nm smaller d_{va} than the larger ones at $d_m = 80$ – 200 nm consistent with our simulations (Fig. 4, $t/\tau_{0,vis} = 1$) when the smallest aggregates approach faster coalescence. For $d_m = 50$ nm the $n_{va} = 2.6$ (Fig. 7b) and thus very close to full coalescence, consistent with a dynamic shape factor near 1 (Fig. 12 in Kim et al., 2009).

At 600 °C (diamonds) particles with d_m of 50, 80 and 100 nm have almost fully coalesced and follow nicely the slope of the coalescence line $d_m = d_p$ ($n_p = 1$), consistent with TEM pictures (Fig. 2 & Fig. 7e,f in Kim et al., 2009) and also the dynamic shape factor, which is almost 1 (Fig. 12 in Kim et al., 2009). Particles with $d_m = 120$ and 150 nm (diamonds) are not yet fully sintered so they are further away from the coalescence line. Larger aggregates take more time to fully coalesce as pointed out above (Fig. 6 in Eggersdorfer et al., 2011). So the d_{va} exhibits a maximum ($d_m = 100$ nm) as a function of d_m at 600 °C (diamonds). Additionally, the n_{va} is around 1.6 for $d_m = 50$ – 100 nm, hence close to $n_p = 1$ of fully sintered spheres, and 5.3 and 14.9 for $d_m = 120$ and 150 nm, respectively, indicating also that these larger aggregates have not reached full coalescence yet (Fig. 7b). So with the present analysis, quantitative information about aggregate morphology and extent of sintering can be acquired from DMA – APM measurements.

3.6.2 Mass-Mobility Exponent D_{fm} and Prefactor k_m from Mass-Mobility Measurements—

The evolution of D_{fm} and k_m obtained here (Fig. 6) is compared to sintering of silver nanoparticle aggregates (Fig. 6 in Kim et al., 2009). Figure 8 shows the normalized aggregate mass $m/m_{va}\left(m_{va}=\pi d_{va}{}^3/6\right)$ as a function of normalized mobility diameter d_m/d_{va} measured (Kim et al., 2009) by DMA-APM at T = 20 – 600 °C. The silver agglomerates entering the sintering tube furnace were produced at the same conditions and had nearly the same primary particle diameter independent of furnace temperature (Kim et al., 2009). The average d_{va} over all d_m (Fig. 7a) at 20 °C is assumed as the initial primary particle diameter and used to calculate the primary particle mass m_{va} by eq. 8 and k_a and D_a of Fig. 3. The mass-mobility exponent, D_{fm}, and prefactor, k_m, are extracted from the experimental data with the power law of eq. 10 in the range of measured d_m and neglecting experimental error.

Figure 8 (legend) shows that the D_{fm} calculated here is in excellent agreement with that of Kim et al. (2009: Fig. 6). Additionally the prefactor k_m is obtained here with eq. 8 (d_{va}). At 20 (triangles) and 100 °C (circles), D_{fm} is estimated by the present analysis as 2.08 and 2.06, respectively, close to that of DLCA or BCCA agglomerates, D_{fm} = 2.15 (Sorensen, 2011). However, the k_m increased from 1.15 to 1.32 from 20 to 100 °C consistent with the calculated sinter neck formation (Fig. 6b). The D_{fm} increases continuously during sintering from 2.08 at 20 °C (triangles) to almost 3 at 600 °C (diamonds) consistent with the present work (Fig. 6a, circles). Only the fully sintered spheres at d_m = 50, 80 and 100 nm are used to determine D_{fm} = 2.95 at 600 °C (Fig. 7a, diamonds) as with Kim et al. (2009).

The normalization of both aggregate mass, m, and mobility, d_m, with initial primary particle mass m_{va} and diameter d_{va} (at 20 °C) is necessary to obtain the prefactor k_m (eq. 10), which is independent of primary particle size and material density and thus can be compared to other measurements or theory. The normalized prefactor k_m increases for aggregates sintered at higher temperatures and reaches a maximum k_m = 1.74 ± 0.07 (here at T = 200 °C, squares) consistent with Fig. 6b. Sintering at 600 °C (diamonds) results in k_m = 0.88 (Fig. 8) for the sintered particles of d_m = 50 – 100 nm, which should theoretically be one for compact spheres (Fig. 6b). A reason for the deviation might be that only three data points are available. The monotonic increase of D_{fm} and the maximum k_m of 1.74 during Ag aggregate sintering (Fig. 8) are consistent with our multiparticle sintering simulations (Fig. 6).

4 Conclusions

Viscous flow sintering and grain boundary diffusion of agglomerate particles is simulated. The morphology of the resulting aggregates is characterized quantitatively by power laws between mass and radius of gyration (D_f and k_n) and between mass and mobility diameter (D_{fm} and k_m). During sintering, the exponent D_{fm} increases monotonically to the limit of 3, while D_f goes first through a minimum, which is attributed to faster sintering of smaller aggregates before reaching 3. So D_{fm} can be used to characterize the degree or extent of aggregate sintering.

A power law between normalized projected aggregate area and average number of primary particles is found in the free molecular and transition regime, where most of sintering and aggregate formation typically take place at high temperature processes. This law is independent of time, material properties and the sintering mechanisms studied here. So it is used to estimate the average primary particle diameter and number from aggregate mass or volume and mobility diameter, data typically obtained by *in-situ* DMA-APM measurements of gas-borne nanoparticles. The primary particle diameters determined with the current method are consistent with counting of particles in electron micrographs. The average

primary particle diameter by DMA-APM measurements can also be directly compared to surface-related measurements like nitrogen adsorption and dynamic light scattering (Sorensen, 2001).

Further work will focus on the evolution of the 3-phase boundaries which are often the most chemically active sites in the particle neck region during sintering. The aim is to develop proper tools for optimizing the activity of nanoparticles.

Acknowledgments

Financial support by ETH Research Grant (ETHIIRA) ETH-11 09-1 and the European Research Council is gratefully acknowledged. This paper received the Best Poster Award on aerosol fundamentals at the European Aerosol Conference in Manchester, UK, September 4-8, 2011.

Appendix

5 Appendix A:

During particle sintering by viscous flow or grain boundary diffusion, particle centers approach each other to reduce their surface area conserving, however, their total volume *v*. The sintering models are set up to solve the change in particle distance dx/dt and the accompanied particle growth rate dr_p/dt by energy and volume balances (Eggersdorfer et al., 2011).

A.1 Viscous sintering

The driving force for sintering is the minimization of free energy by reduction of particle surface area. The energy gained by surface reduction is dissipated by viscous flow setting the timescale for sintering. The viscous flow is extensional (Frenkel, 1945) that results in approaching particle centers so the spherical particles overlap. The overlapping volume is counted only once and the particle radius is increased to conserve particle volume (Kadushnikov et al., 2001). The characteristic sintering time for viscous sintering is (Frenkel, 1945):

$$\tau_{0,vis}=\frac{\eta r_{p,0}}{\gamma}, \quad \text{(A1)}$$

where η is the viscosity and γ the surface energy. The detailed multiparticle viscous sintering model is described by Eggersdorfer et al. (2011).

A.2 Grain boundary diffusion

Nanoparticles in contact with two misaligned crystals form a grain boundary at their neck. Atoms diffuse from the neck center (source) to its surface (sink). The driving force for diffusion is the stress gradient between neck center and surface caused by the particle curvature in the neck (Chiang et al., 1997). The flux of atoms J into the neck is (Coble, 1958):

$$J=\frac{D_v}{\Omega}\frac{dC_v}{dR}, \quad \text{(A2)}$$

where dC_V/dR is the vacancy concentration gradient and C_V is the fraction of sites occupied by vacancies.

The volume of material transported through the neck area, $a_n = \pi R^2$, into the neck per time is:

$$\frac{dv}{dt} = a_n \frac{dx}{dt} = J a_{gb} \Omega, \quad \text{(A3)}$$

where $a_{gb} = 2\pi R \delta_{gb}$ is the cylindrical, cross sectional area over which diffusion occurs and δ_{gb} is the grain boundary thickness. The vacancy concentration between the neck surface and center of neck is assumed constant (Rahaman, 2008): $dC_v/dR = \Delta C_v/R$, with

$$\Delta C_v = C_v - C_{v0} = C_{v0}\left(\exp\left(-\frac{\gamma\Omega}{k_B T}\left(\frac{1}{R_{out}} - \frac{1}{R}\right)\right) - 1\right), \quad \text{(A4)}$$

where $R_{out} = r_1 - x_1$ is the outer neck radius (Coble, 1958). Typically, $\gamma\Omega\left(\frac{1}{R_{out}} - \frac{1}{R}\right) \ll k_B T$ and the exponential function is approximated as $C_v = C_{v0}\left(1 - \frac{\gamma\Omega}{k_B T}\left(\frac{1}{R_{out}} - \frac{1}{R}\right)\right)$, which results in a vacancy concentration difference:

$$\Delta C_v = -C_{v0}\frac{\gamma\Omega}{k_B T}\left(\frac{1}{R_{out}} - \frac{1}{R}\right). \quad \text{(A5)}$$

Equations A2 and A5 are substituted into eq. A3 to determine the rate of shrinkage dx/dt^*:

$$\frac{dx}{dt^*} = -\frac{r_{p,0}^4}{a_n}\left(\frac{1}{R_{out}} - \frac{1}{R}\right). \quad \text{(A6)}$$

with the dimensionless time $t^* = t/\tau_{0,gb}$:

$$\tau_{0,gb} = \frac{k_B T r_{p,0}^4}{2\pi D_v C_{v0} \delta_{gb} \gamma \Omega}, \quad \text{(A7)}$$

where $r_{p,0}$ is the initial primary particle radius. The diffusion coefficient is expressed, at least over some limited temperature range, as a thermally activated process (Chiang et al., 1997):

$$D_v = D_{v0} \exp\left(\frac{-Q}{N_A k_B T}\right), \quad \text{(A8)}$$

where D_{v0} is a constant, Q is an experimentally determined activation energy and N_A is the Avogadro number. Thus the diffusion coefficient dominates the temperature dependence of $\tau_{0,gb}$. The initial orientations of crystal lattices influence the sintering behavior (Theissmann et al., 2008). This effect is not accounted for in this model but is included by using an effective or average diffusion coefficient.

A.3 Multi-particle sintering

The change in center-to-center distance is calculated separately for all particle pairs in contact (eq. A6). The neck area a_n and angle (2π in eq. A7) are determined with the Vorlume software (Cazals et al., 2011) to account for multiple particle overlaps which result in non-spherical contact areas and angles below 2π. The volume (mass) conservation is calculated as described in Eggersdorfer et al. (2011). The outer neck radius R_o of unequally

sized particles is chosen as the overlap individually for each particle in contact (Coble, 1958).

7 Nomenclature

a	surface area, m^2
B	auxiliary variable for eq. 11
C_v	fraction of sites occupied by vacancies
$D_{a/f/fm}$	scaling exponents for eq. 3, 4, 6, 9, 10
D_v	vacancy diffusion coefficient, $m^2\ s^{-1}$
d	diameter, m
J	flux of atoms, $\#\ s^{-1}\ m^{-5}$
k_B	Boltzmann constant, $m^2\ kg\ s^{-2}\ K^{-1}$
$k_{a/f/fm/n/m}$	prefactors for eq. 3, 4, 6, 9, 10
m	mass, kg
N_A	Avogadro number, mol^{-1}
n	number
Q	activation energy, $J\ mol^{-1}$
R	neck radius, m
r_g	radius of gyration, m
r	radius, m
T	temperature, K
t	time, s
t^*	dimensionless time
v	volume, m^3
w	scaling eq. 11
x	particle center to neck distance, m
y	scaling eq. 11
z	coordination number

Greek letters

γ	surface energy, $kg\ s^{-2}$
δ_{gb}	grain boundary thickness, m
η	viscosity, $kg\ s^{-1}\ m^{-1}$
ρ	density, $kg\ m^{-3}$
τ	characteristic sintering time, s
Ω	volume of atom or vacancy, m^3

Europe PMC Funders Author Manuscripts

Subscripts

0	initial
a	average projected
gb	grain boundary
m	mobility
n	neck
out	outer
p	primary particle
va	volume and surface equivalent
vis	viscous

8 References

Akhtar MK, Lipscomb GG, Pratsinis SE. Monte-Carlo simulation of particle coagulation and sintering. Aerosol Science and Technology. 1994; 21:83–93.

Al Zaitone B, Schmid HJ, Peukert W. Simulation of structure and mobility of aggregates formed by simultaneous coagulation, sintering and surface growth. Journal of Aerosol Science. 2009; 40:950–964.

Botet R, Jullien R, Kolb M. Hierarchical model for irreversible kinetic cluster formation. Journal of Physics A: Mathematical and General. 1984; 17:L75–L79.

Buesser B, Grohn AJ, Pratsinis SE. Sintering rate and mechanism of TiO_2 nanoparticles by molecular dynamics. Journal of Physical Chemistry C. 2011; 115:11030–11035.

Camenzind A, Schulz H, Teleki A, Beaucage G, Narayanan T, Pratsinis SE. Nanostructure evolution: From aggregated to spherical SiO_2 particles made in diffusion flames. European Journal of Inorganic Chemistry. 2008:911–918.

Cazals F, Kanhere H, Loriot S. Computing the volume of a union of balls: a robust algorithm. ACM Transactions on Mathematical Software. 2011:38.

Chiang, YM.; Birnie, DP.; Kingery, WD. Physical Ceramics. John Wiley & Sons; New York: 1997.

Coble RL. Initial sintering of alumina and hematite. Journal of the American Ceramic Society. 1958; 41:55–62.

Eggersdorfer ML, Kadau D, Herrmann HJ, Pratsinis SE. Fragmentation and restructuring of soft-agglomerates under shear. Journal of Colloid and Interface Science. 2010; 342:261–268. [PubMed: 19948345]

Eggersdorfer ML, Kadau D, Herrmann HJ, Pratsinis SE. Multiparticle sintering dynamics: from fractal-like aggregates to compact structures. Langmuir. 2011; 27:6358–6367. [PubMed: 21488641]

Eggersdorfer ML, Pratsinis SE. The Structure of Agglomerates consisting of Polydisperse Particles. Aerosol Science and Technology. 2012; 46:347–353.

Ehara K, Hagwood C, Coakley KJ. Novel method to classify aerosol particles according to their mass-to-charge ratio - Aerosol particle mass analyser. Journal of Aerosol Science. 1996; 27:217–234.

Filippov AV, Zurita M, Rosner DE. Fractal-like aggregates: Relation between morphology and physical properties. Journal of Colloid and Interface Science. 2000; 229:261–273. [PubMed: 10942568]

Frenkel J. Viscous Flow of Crystalline Bodies under the Action of Surface Tension. Journal of Physics (USSR). 1945; 9:385–391.

Hasmy A, Foret M, Pelous J, Jullien R. Small-angle neutron-scattering investigation of short-range correlations in fractal aerogels - simulations and experiments. Physical Review B. 1993; 48:9345–9353.

Heine MC, Pratsinis SE. Agglomerate TiO_2 aerosol dynamics at high concentrations. Particle & Particle Systems Characterization. 2007; 24:56–65.

Heinson WR, Sorensen CM, Chakrabarti A. Does shape anisotropy control the fractal dimension in diffusion-limited cluster-cluster aggregation? Aerosol Science and Technology. 2010; 44:I–IV.

Hiemenz, PC. Principles of Colloid and Surface Chemistry. Marcel Dekker. Inc.; New York: 1986. p. 42

Hyeon-Lee J, Beaucage G, Pratsinis SE, Vemury S. Fractal analysis of flame-synthesized nanostructured silica and titania powders using small-angle X-ray scattering. Langmuir. 1998; 14:5751–5756.

Jullien, R.; Botet, R. Aggregation and fractal aggregates. World Scientific; River Edge: 1987.

Kadushnikov RM, Skorokhod VV, Kamenin IG, Alievskii VM, Nurkanov EY, Alievskii DM. Computer simulation of spherical particle sintering. Powder Metallurgy and Metal Ceramics. 2001; 40:154–163.

Keskinen H, Tricoli A, Marjamaki M, Makela JM, Pratsinis SE. Size-selected agglomerates of SnO_2 nanoparticles as gas sensors. Journal of Applied Physics. 2009; 106:084316.

Kim SC, Wang J, Emery MS, Shin WG, Mulholland GW, Pui DYH. Structural Property Effect of Nanoparticle Agglomerates on Particle Penetration through Fibrous Filter. Aerosol Science and Technology. 2009; 43:344–355.

Knutson EO, Whitby KT. Aerosol classification by electric mobility: apparatus, theory, and applications. Journal of Aerosol Science. 1975; 6:443–451.

Koch W, Friedlander SK. The effect of particle coalescence on the surface-area of coagulating aerosol. Journal of Colloid and Interface Science. 1990; 140:419–427.

Kolb M, Herrmann HJ. Surface fractals in irreversible aggregation. Physical Review Letters. 1987; 59:454–457. [PubMed: 10035773]

Koylu UO, Faeth GM. Structure of overfire soot in buoyant turbulent-diffusion flames at long residence times. Combustion and Flame. 1992; 89:140–156.

Kruis FE, Kusters KA, Pratsinis SE, Scarlett B. A simple-model for the evolution of the characteristics of aggregate particles undergoing coagulation and sintering. Aerosol Science and Technology. 1993; 19:514–526.

Lall AA, Friedlander SK. On-line measurement of ultrafine aggregate surface area and volume distributions by electrical mobility analysis: 1. Theoretical analysis. Journal of Aerosol Science. 2006; 37:260–271.

Mandelbrot, BB. The fractal geometry of nature. W.H. Freeman; San Francisco: 1982.

Meakin P. Fractal aggregates. Advances in Colloid and Interface Science. 1988; 28:249–331. [PubMed: 2577851]

Medalia AI. Morphology of aggregates .1. Calculation of shape and bulkiness factors - application to computer-simulated random flocs. Journal of Colloid and Interface Science. 1967; 24:393–404.

Megaridis CM, Dobbins RA. Morphological description of flame-generated materials. Combustion Science and Technology. 1990; 71:95–109.

Park K, Cao F, Kittelson DB, McMurry PH. Relationship between particle mass and mobility for diesel exhaust particles. Environmental Science & Technology. 2003; 37:577–583. [PubMed: 12630475]

Park K, Kittelson DB, McMurry PH. Structural properties of diesel exhaust particles measured by transmission electron microscopy (TEM): Relationships to particle mass and mobility. Aerosol Science and Technology. 2004; 38:881–889.

Rahaman, MN. Sintering of Ceramics. CRC Press; Boca Raton: 2008.

Riefler N, Madler L. Structure-conductivity relations of simulated highly porous nanoparticle aggregate films. Journal of Nanoparticle Research. 2010; 12:853–863.

Rogak SN, Flagan RC, Nguyen HV. The mobility and structure of aerosol agglomerates. Aerosol Science and Technology. 1993; 18:25–47.

Schaefer DW, Hurd AJ. Growth and structure of combustion aerosols - fumed silica. Aerosol Science and Technology. 1990; 12:876–890.

Scheckman JH, McMurry PH, Pratsinis SE. Rapid characterization of agglomerate aerosols by in situ mass-mobility measurements. Langmuir. 2009; 25:8248–8254. [PubMed: 19594189]

Sorensen CM. Light scattering by fractal aggregates: A review. Aerosol Science and Technology. 2001; 35:648–687.

Sorensen CM. The mobility of fractal aggregates: A review. Aerosol Science and Technology. 2011; 45:755–769.

Sorensen CM, Cai J, Lu N. Light-scattering measurements of monomer size, monomers per aggregate, and fractal dimension for soot aggregates in flames. Applied Optics. 1992; 31:6547–6557. [PubMed: 20733873]

Strobel R, Pratsinis SE. Flame aerosol synthesis of smart nanostructured materials. Journal of Materials Chemistry. 2007; 17:4743–4756.

Sutherland DN, Goodarz-Nia I. Floc simulation - Effect of collision sequence. Chemical Engineering Science. 1971; 26:2071–2085.

Tence M, Chevalier JP, Jullien R. On the measurement of the fractal dimension of aggregated particles by electron-microscopy - experimental-method, corrections and comparison with numerical-models. Journal De Physique. 1986; 47:1989–1998.

Theissmann R, Fendrich M, Zinetullin R, Guenther G, Schierning G, Wolf DE. Crystallographic reorientation and nanoparticle coalescence. Physical Review B. 2008; 78:205413.

Tricoli A, Graf M, Mayer F, Kuhne S, Hierlemann A, Pratsinis SE. Micropatterning layers by flame aerosol deposition-annealing. Advanced Materials. 2008a; 20:3005–3010.

Tricoli A, Graf M, Pratsinis SE. Optimal doping for enhanced SnO_2 sensitivity and thermal stability. Advanced Functional Materials. 2008b; 18:1969–1976.

Tsantilis S, Pratsinis SE. Soft- and hard-agglomerate aerosols made at high temperatures. Langmuir. 2004; 20:5933–5939. [PubMed: 16459612]

Tsyganov S, Kastner J, Rellinghaus B, Kauffeldt T, Westerhoff F, Wolf DE. Analysis of Ni nanoparticle gas phase sintering. Physical Review B. 2007; 75:045421.

Ulrich GD. Flame synthesis of fine particles. Chemical and Engineering News. 1984; 62(32):22–29. [PubMed: 11541976]

Wolf, DE.; Brendel, L.; Fendrich, M.; Zinetullin, R. Nanopowder Sintering. In: Lorke, L.; Winterer, M.; Schmechel, R.; Schulz, C., editors. Nanoparticles from the Gasphase: Formation – Structure – Properties. Springer; Heidelberg: 2012.

Xiong Y, Akhtar MK, Pratsinis SE. Formation of agglomerate particles by coagulation and sintering. 2. The evolution of the morphology of aerosol-made titania, silica and silica-doped titania powders. Journal of Aerosol Science. 1993; 24:301–313.

Xiong Y, Pratsinis SE. Formation of agglomerate particles by coagulation and sintering. 1. A 2-dimensional solution of the population balance equation. Journal of Aerosol Science. 1993; 24:283–300.

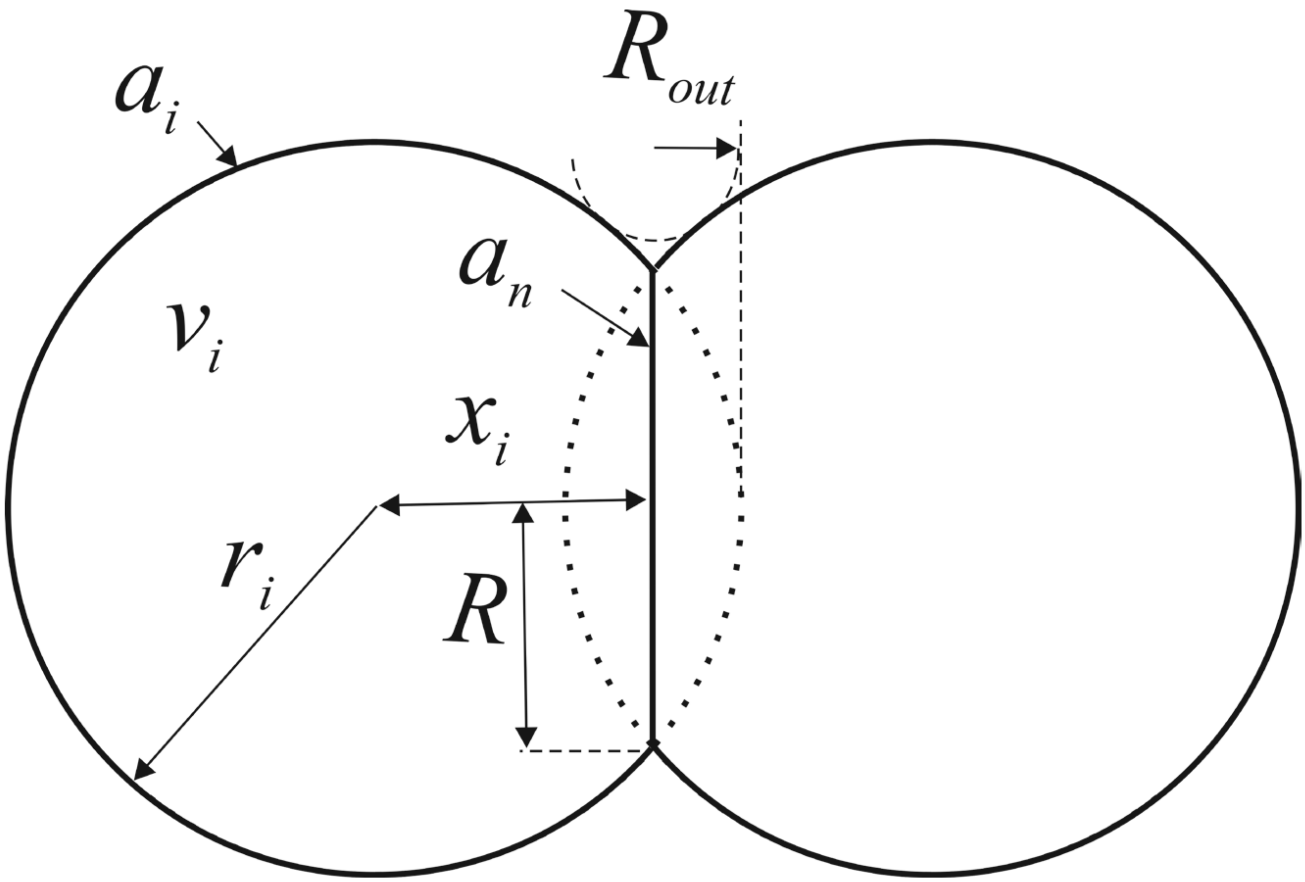

Figure 1.
A two dimensional sketch of a pair of spherical particles during sintering.

Europe PMC Funders Author Manuscripts

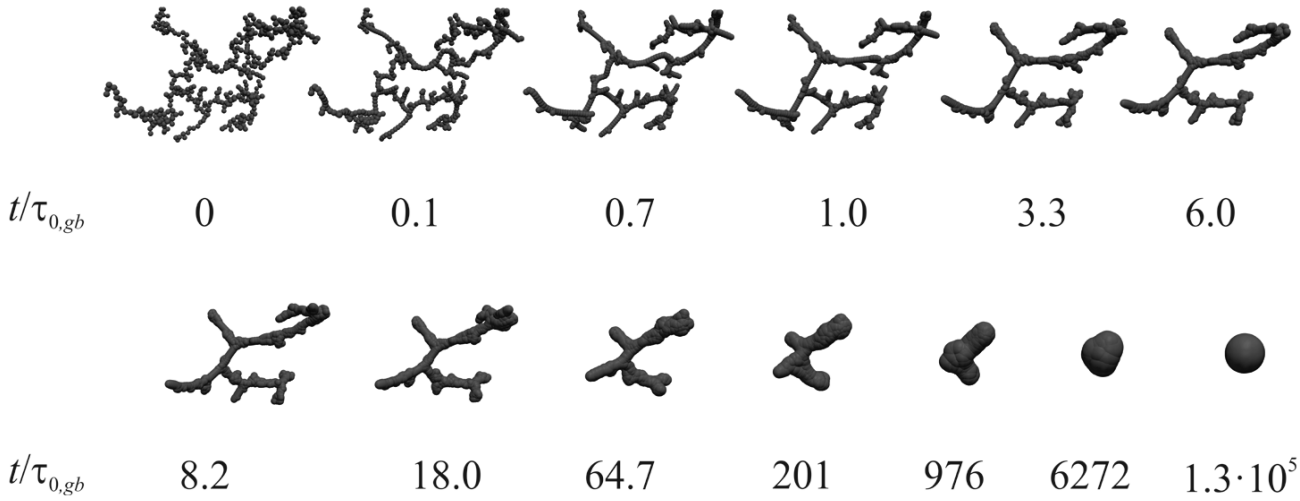

Figure 2.
Snapshots of an aggregate undergoing sintering by grain boundary diffusion that was initially made by diffusion-limited cluster-cluster (DLCA) agglomeration of 512 primary particles.

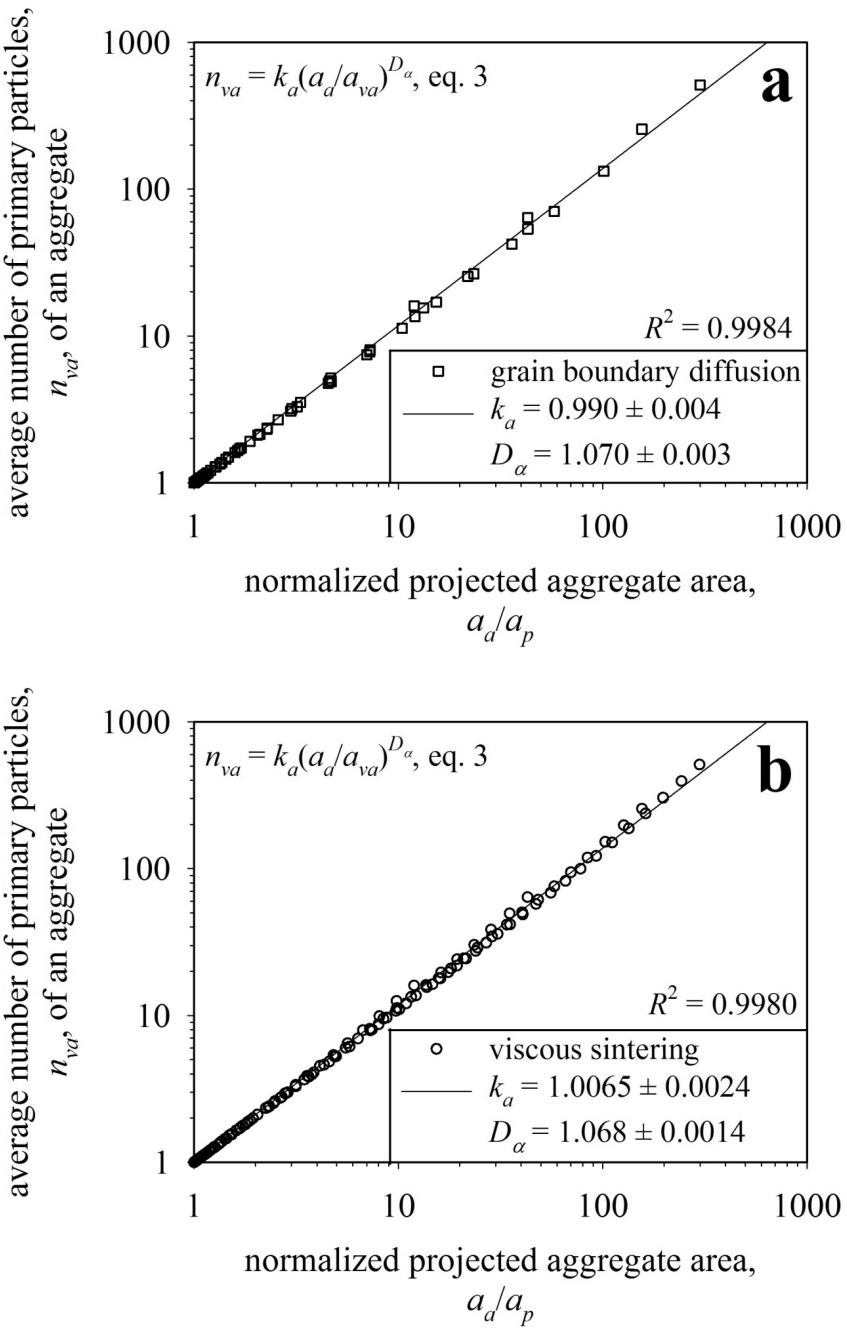

Figure 3.
A power law (eq. 3) holds between normalized projected aggregate area a_d/a_p and average number of primary particles n_{va} during sintering by a) grain boundary diffusion and b) viscous flow. The differences of k_a and D_α between the two sintering mechanisms are small so averages can be taken for application to experimental data ($k_a = 0.998$, $D_\alpha = 1.069$, see Fig 7).

Europe PMC Funders Author Manuscripts

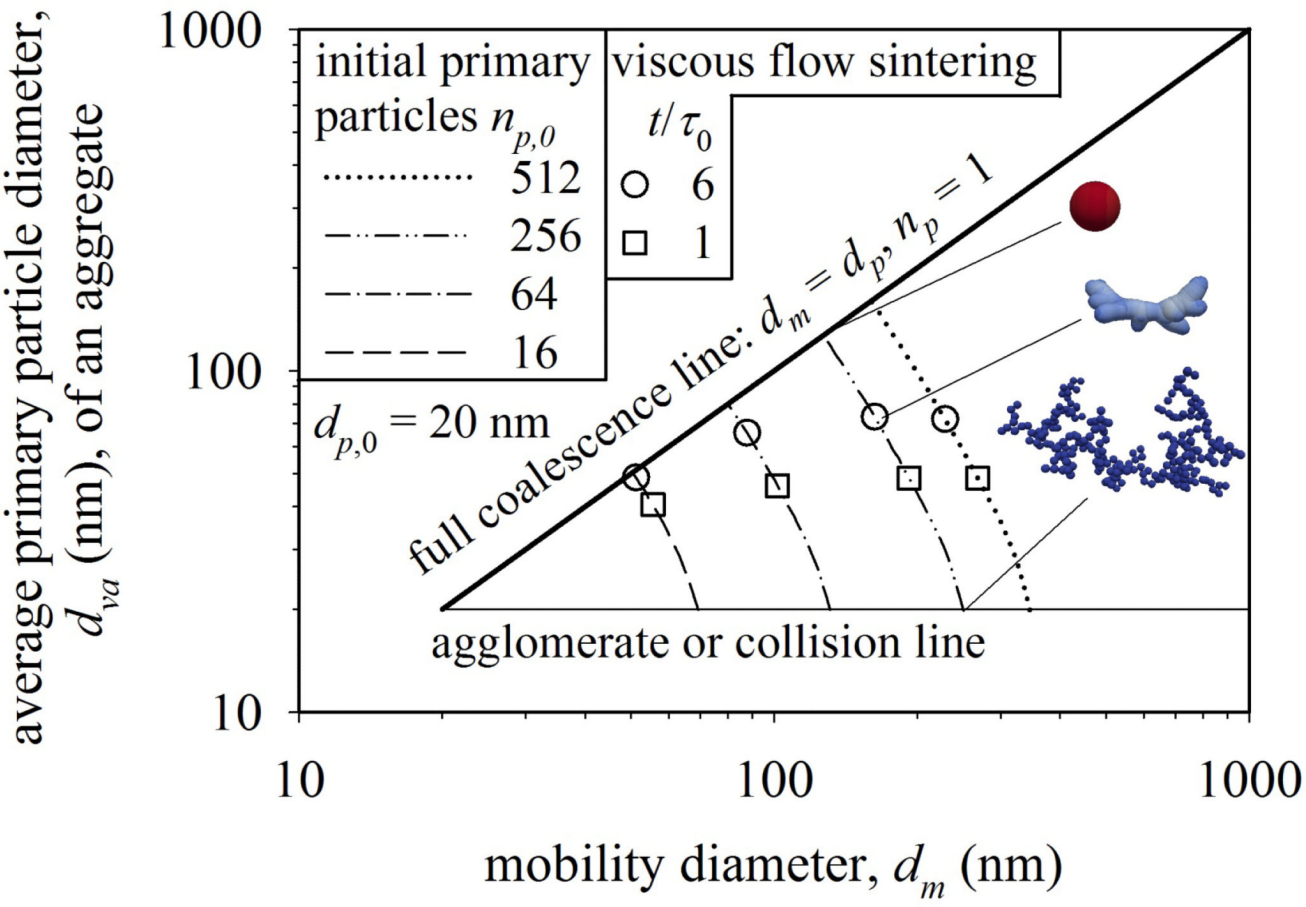

Figure 4.

The evolution of the average primary particle diameter, d_{va}, as a function of aggregate mobility diameter, d_m, during sintering of agglomerates with initially 16 (broken line), 64 (dot-broken line), 256 (double-dot broken line) and 512 (dotted line) primary particles of 20 nm initial diameter. For agglomerates of monodisperse spherical primary particles, $d_{va} = d_p$ independent of mobility size, given by the thin horizontal agglomerate or collision line. The mobility diameter decreases during sintering while d_{va} increases until a compact particle ($D_f = 3$) is reached (bold diagonal coalescence line). The relation between d_{va} and d_m is independent of time, material properties or sintering mechanism. The progress of sintering at $t/\tau_0 = 1$ (squares) and 6 (circles) is shown for viscous sintering.

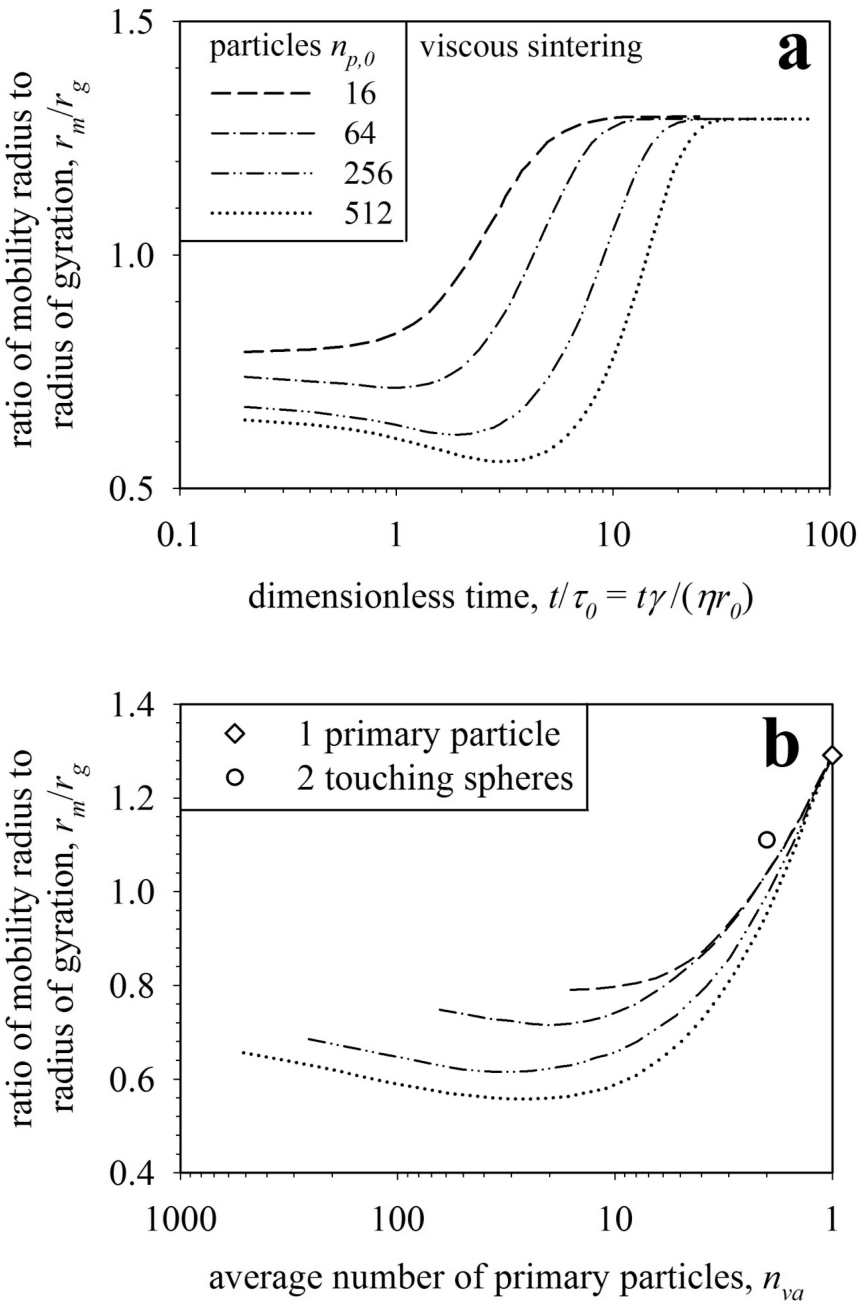

Figure 5.

The ratio between mobility radius to radius of gyration, r_m/r_g, as a function of normalized time, t/τ_0 (a), and average number of primary particles, n_{va} (b), during sintering of aggregates containing initially 16, 64, 256 and 512 primary particles. The ratio r_m/r_g converges to the theoretical limit of $\sqrt{5/3}$ for full coalescence (n_{va} = 1, Hiemenz, 1986). Although the r_m/r_g limit for full coalescence to a single particle is obtained (diamond), the theoretical limit for a two particle agglomerate (circle) is not reached because the sintering particles have an oval shape and not that of two spheres with a point contact (Fig. 2, $t/\tau_{0,gb}$ = 6272).

Europe PMC Funders Author Manuscripts

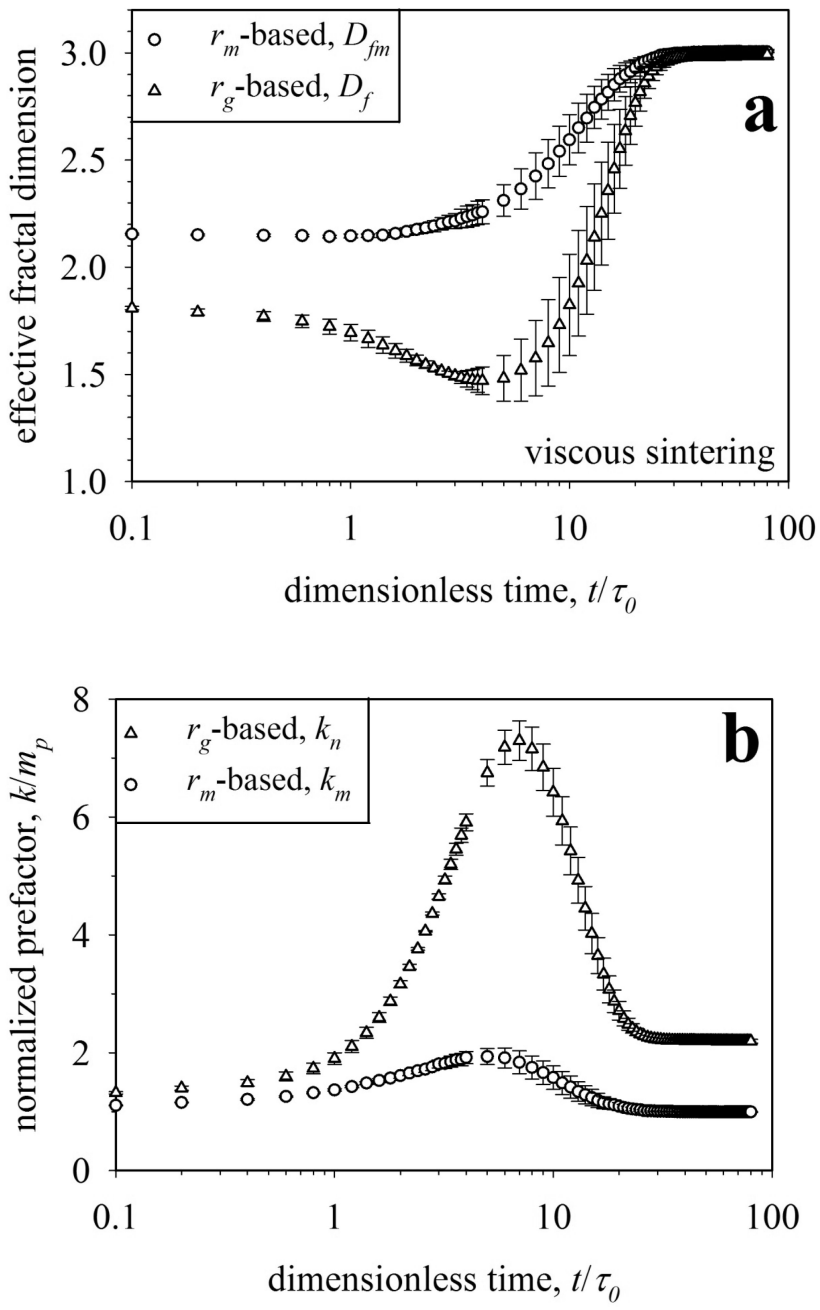

Figure 6.

The temporal evolution of the effective fractal dimension (D_f, eq. 6) and mass-mobility exponent (D_{fm}, eq. 10) (a) and prefactors (b) during viscous sintering of agglomerates having initially 16 – 512 primary particles. The exponents (D_f, D_{fm}) and prefactors (k_n, k_m) are obtained by ensemble averaging over 50 agglomerates of each size. Only D_{fm} exhibits monotonic behavior and thus can be used to characterize the degree or extent of sintering of aggregates.

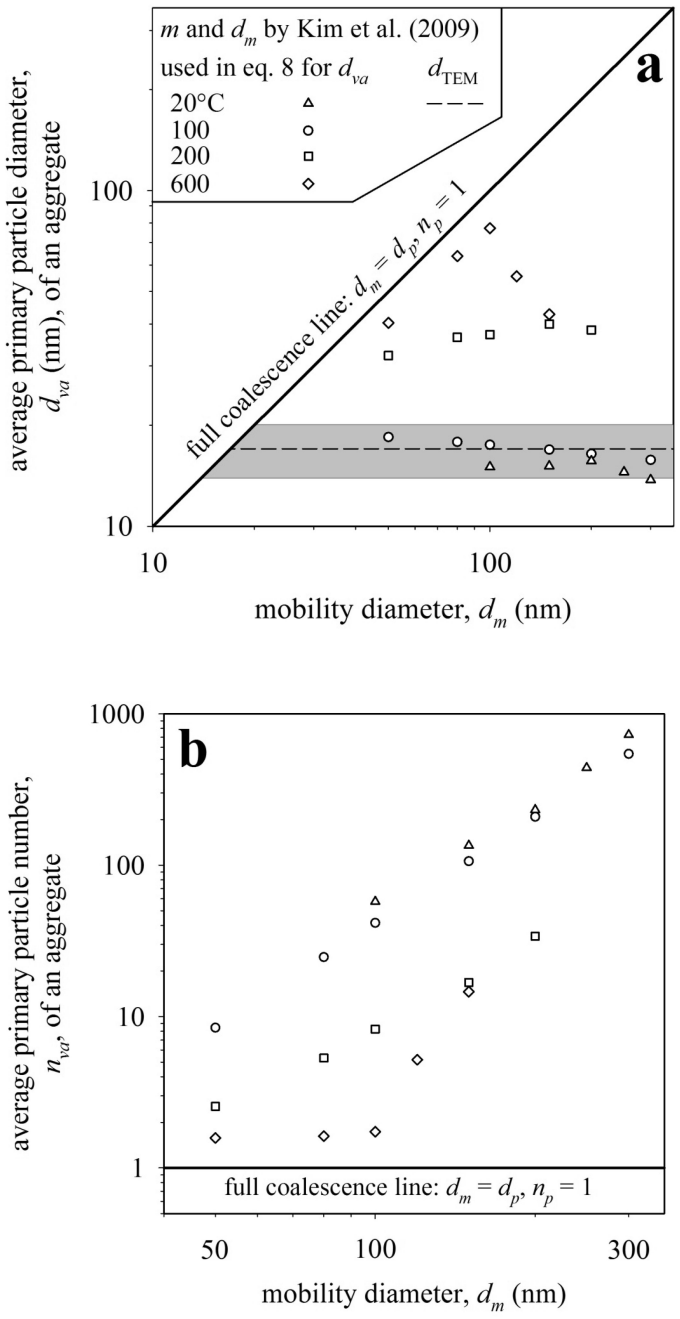

Figure 7.

The average primary particle diameter, d_{va} (a), and number, n_{va} (b), of silver nanoparticle agglomerates by Kim et al. (2009) is estimated by eq. 2 & 8 for different sintering temperatures. The broken line represents the primary particle diameter d_{TEM} obtained by TEM and converted to surface-average mean diameter. The d_{va} by eq. 8 is within the error bars (grey area) of d_{TEM} and is independent of mobility diameter. Higher furnace temperatures (T = 200 – 600 °C) lead to faster sintering, larger d_{va} and less n_{va}.

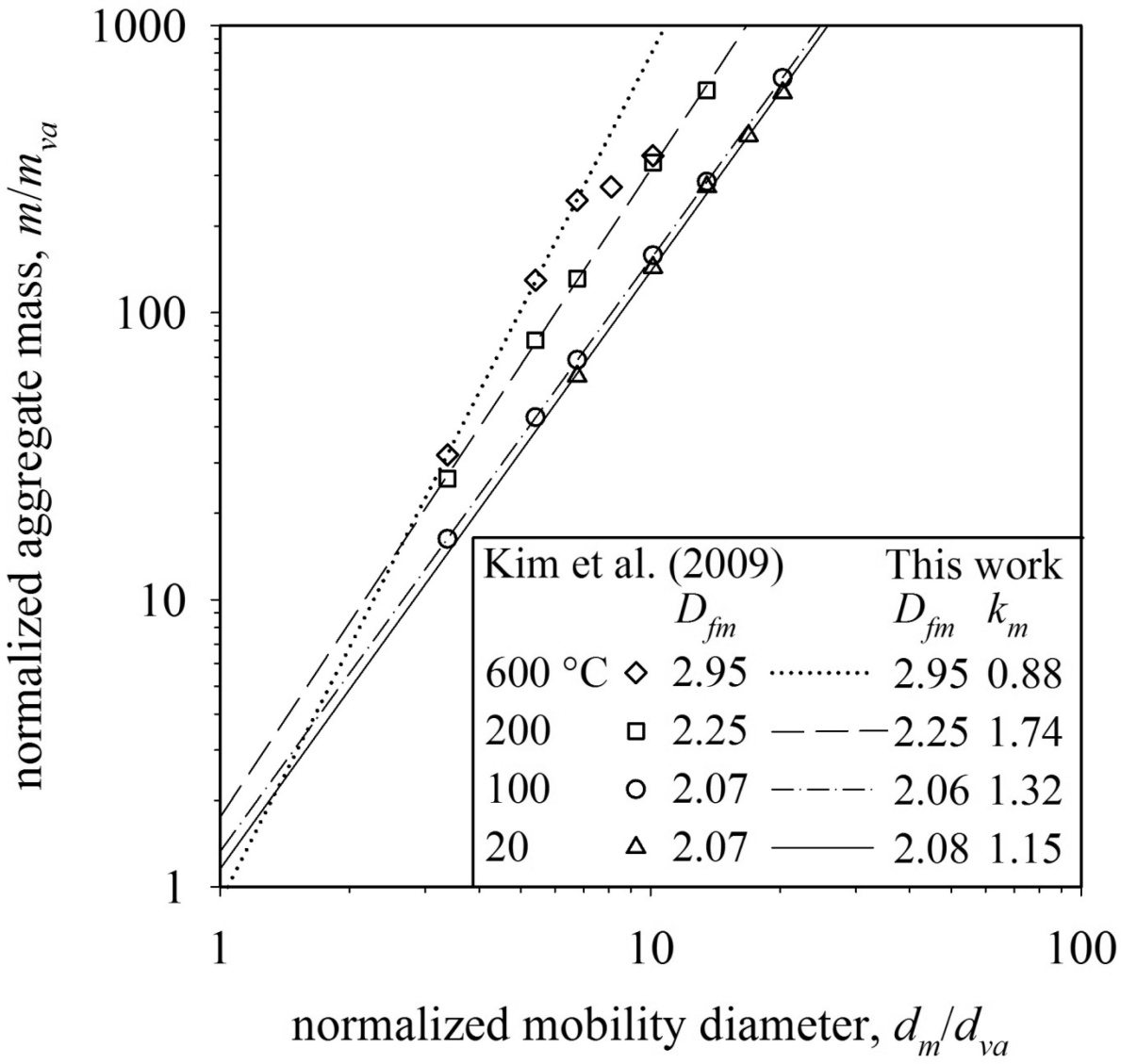

Figure 8.

The DMA-APM data of silver nanoparticle aggregates sintered at different temperatures ranging from 20 to 600 °C by Kim et al. (2009) are post-processed here and the exponent D_{fm} and prefactor k_m of eq. 10 are determined. At T = 20 the D_{fm} and k_m are in agreement with agglomerates from the present simulations (D_{fm} = 2.15 and k_m = 1.11). Higher furnace temperatures result in faster sintering and also more compact structures. At T = 600°C the aggregates with d_m = 50, 80 and 100 nm have almost fully coalesced (D_{fm} = 2.95, k_m = 0.88) while the larger ones lag behind. A maximum in k_m is found here at T = 200°C consistent with the present work (Fig. 6b).